Materials Advances

ROYAL SOCIETY OF CHEMISTRY

PAPER

View Article Online
View Journal | View Issue

Cite this: *Mater. Adv.*, 2026, 7, 265

Thermal evaporation fabrication of UV-NIR p–i–n photodetectors based on highly tensile-strained Ge *via* incorporation of Pb rather than Sn and As

Mohamed A. Nawwar,*[a] Abdelhamid El-Shaer,[b] Mohamed Y. Saeed,[a] Magdy S. Abo Ghazala,[a] Ahmed Mourtada Elseman[c] and Abd El-Hady B. Kashyout*[d]

Direct band gap strained germanium (Ge) is one of the promising materials that have been used in various applications in the last decades, with elements such as Sn, As, and Pb being used to modulate the Ge band gap. In this work, we compared the effect of the content of three metals (Sn, As, and Pb) on the Ge structure and optoelectronic properties and demonstrated the advantages of Pb content over Sn. We fabricated p–i–n based poly-Ge by Sn-, As-, and Pb-induced crystallization of thermally deposited Ge annealed at 400 °C under vacuum. Raman spectroscopy and X-ray diffraction were used to investigate the impact of the incorporation of metals on the strain in the Ge network. We investigated the direct transition of the prepared samples using UV-Vis-NIR spectroscopy and photoluminescence. We measured the charge carrier lifetime using time-resolved PL. We investigated the diode quality and dark current using *I–V* characteristics in dark conditions. Photoresponsivity measurements were performed to measure the spectral response of the prepared junctions. The results reveal that the GePb-based p–i–n junction has a higher tensile strain than GeAs and GeSn. GePb has many direct transitions in the UV, NIR, and mid-IR regions of the spectra. GePb has a longer carrier lifetime than GeSn and a low dark current and a quality factor near the ideal value compared to the other prepared junctions. The fabricated GePb-based photodetector (PD) has a higher responsivity in the UV and NIR regions compared to GeSn- and GeAs-based PDs. This makes the fabricated GePb-based PD more suitable than GeSn for photodetection applications in multiple regions of the spectrum.

Received 21st August 2025,
Accepted 14th November 2025

DOI: 10.1039/d5ma00940e

rsc.li/materials-advances

Introduction

Germanium has recently attracted great interest because it is used in optoelectronics, photonics, and infrared telecommunication applications.[1] Unfortunately, Ge has an indirect band gap that is not preferred in emission and detection applications.[2] There are many ways to modulate the Ge band gap, including indirect and direct methods, such as strain engineering in the Ge network and incorporation of large metal atoms such as Sn and Pb.[3] GeSn alloys have been studied more extensively than GePb compounds since Pb has a lower solubility in Ge than Sn because of the lattice mismatch with Ge.[4] Thus, few trials have examined the incorporation of Pb inside Ge networks. Single-crystalline GePb was prepared for the first time by Qian Zhou *et al.*, who used pulsed laser-induced epitaxy followed by laser annealing to generate a GePb compound with 3% Pb content.[5] M. C. J. Weiser *et al.* used different fluencies of the pulsed laser to incorporate Pb inside the Ge network. They investigated the impact of laser fluencies using Raman spectroscopy.[6] Single-crystalline GePb alloys were prepared for the first time *via* magnetron sputtering by Xiangquan Liu *et al.*[7] Jiayin Yang *et al.* used a 2×10^{15} cm^{-2} implantation dose with an energy of 20 keV followed by rapid thermal annealing at 400 °C, 550 °C, and 700 °C to obtain good-quality GePb crystals.[8] Hakimah Alahmad *et al.* employed Pb-induced crystallization of thermally evaporated amorphous Ge for the first time to obtain (004) GePb crystallites.[9] Xiangquan Liu *et al.* reported another trial in which they prepared GePb/Ge multiple quantum wells to enhance the radiative emission *via* quantum confinement.[10] Theoretical investigations of the GePb band structure and optical and

[a] *Physics Department, Faculty of Science, Menoufia University, Shebin El-Koom, Menoufia, Egypt. E-mail: mohamed.nawwar@science.menofia.edu.eg*
[b] *Physics Department, Faculty of Science, Kafrelsheikh University, KafrelSheikh 33516, Egypt*
[c] *Electronic & Magnetic Materials Department, Central Metallurgical Research & Development Institute (CMRDI), 11421 Helwan, Cairo, Egypt*
[d] *Electronic Materials Department, Advanced Technology and New Materials Research Institute, City of Scientific Research and Technological Applications (SRTA-City), New Borg El-Arab City, Alexandria, Egypt. E-mail: akashyout@srtacity.sci.eg*

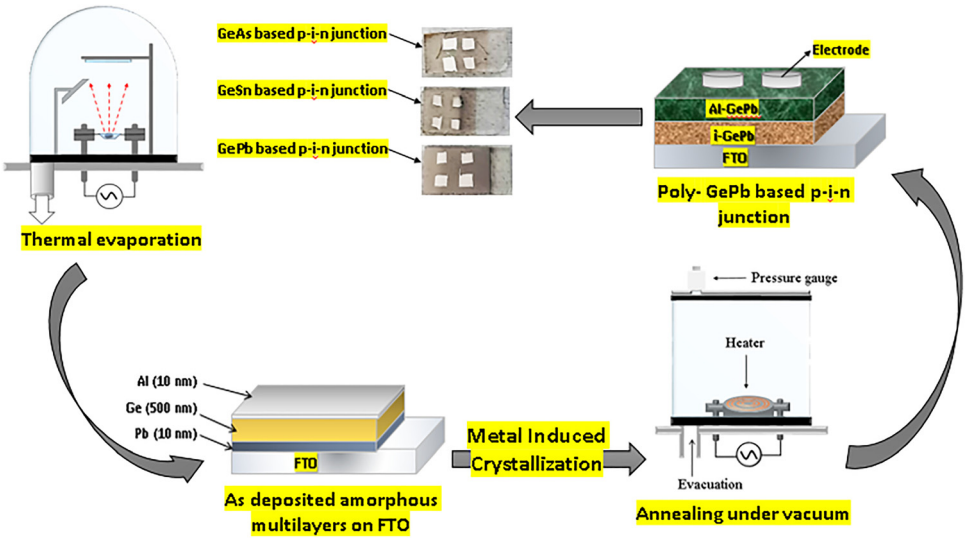

Fig. 1 Schematic of the fabrication of p–i–n based poly-Ge junctions *via* MIC.

electronic properties using the Broyden–Fletcher–Goldfarb–Shanno (BFGS) algorithm have been demonstrated.[11,12] Xiangquan Liu *et al.* also fabricated a p-GePb/i-GePb/n-Ge photodetector with a dark current of value 10^{-3} to 10^{-4} A and a cut-off photoresponsivity at 1600 nm.[13] Jiulong Yu *et al.* fabricated a p-Ge/GePb/n-Ge photodetector with a SiO_2 passivation layer. This p–i–n GePb photodetector exhibited a dark current of 10^{-6} A and a cut-off photoresponsivity at 1800 nm.[14]

In this work, we were motivated to find a way to replace Sn with Pb and consequently obtain a germanium alloy with a highly strained, directly tunable band gap, and to utilize the GePb alloy in the fabrication of optoelectronic devices using fluorine-doped tin oxide (FTO)/glass as the substrate. The band gap of the GePb compound can be adjusted by changing the Pb content. This work is mainly aimed at overcoming the low solubility of Pb in germanium by using the MIC process to generate a highly strained direct band gap Ge crystalline thin film with lower dark current and higher responsivity in the NIR region compared to the Ge thin films doped with Sn or As. We also employed low-vacuum annealing during the MIC process to facilitate the oxidation of germanium. This results in band-to-band transition corresponding to GeO_2 in the UV region of the spectra, in addition to the response of Ge with Pb content in the NIR region. The fabricated p–i–n junctions constructed by this technique are the first GePb junctions to exhibit photoresponsivity peaks in both UV and NIR regions.

We performed comparative experimental studies on GeAs, GeSn, and GePb alloys that were prepared by metal-induced crystallization of thermally evaporated a-Ge thin films. We investigated the higher strain effect of Pb content rather than Sn or As. We confirmed the advantages of using Pb over Sn for the preparation of direct transition strained Ge. We then studied the effects of the annealing time on the optical band gap, decay lifetime, dark current, and photoresponsivity of the fabricated p–i–n based GePb photodetectors.

Experimental procedures

Thermal deposition of metal/semiconductor multilayers

Three different semiconductor and metal layer configurations were deposited on the fluorine-doped tin oxide (FTO)/glass substrates using the thermal vacuum evaporation technique (Edwards E306A). The fabricated layers were deposited under a vacuum of 6.5×10^{-5} mbar as follows: a 50 nm layer of As, Sn, or Pb was deposited separately on FTO/glass substrates. Then, each metal layer was covered with a 500 nm layer of Ge followed by 10 nm of Al as a p-dopant on Ge/(metal layer) above the n-type FTO substrates (see Fig. 1).

Fabrication of p–i–n based poly-Ge junctions *via* metal-induced crystallization (MIC)

The multilayers with different configurations on the above-mentioned substrates were annealed at 400 °C under low-vacuum conditions (4×10^{-2} mbar, Edwards rotary pump) inside a vacuum cylindrical chamber. The deposited Pb/Ge/Al layers were annealed for 1, 3, and 5 hours. The As/Ge/Al layers were annealed for 5 hours, and the Sn/Ge/Al layers were annealed for 5 hours. Metal-induced crystallization of amorphously deposited Ge occurred *via* the incorporation of As, Sn, and Pb separately. Al dopant represents 2% and Pb represents 10% of the 500 nm germanium layer. After the annealing, p–i–n junctions were formed, then Al metal electrodes were deposited for the electrical and photoresponsivity measurements (see Fig. 1).

Investigation of the strained Ge structure obtained *via* the incorporation of As, Sn, and Pb atoms

A Witec alpha300 Raman confocal microscope with an excitation laser wavelength of 352 nm, and a Brucker D8-Advance X-ray diffractometer were employed to investigate the strain in the Ge network introduced by the incorporation of As, Sn, and Pb.

Direct band-gap investigation

Direct transitions and band-gap values of the prepared heterostructures were investigated using a UV-Vis-NIR absorbance spectrophotometer (JASCO, Model V-770) at a range of wavelengths (200–1800 nm), and a photoluminescence spectrometer (PicoQuant) with a 418 nm excitation diode laser source and a UV-Red photomultiplier tube to detect the sample's emission.

Current–potential (*I–V*) characteristics

I–V characteristics of the fabricated junctions and diode parameter calculations were obtained using a potentiostat (Metrohm Autolab 87070).

Charge carrier lifetime

The charge carrier lifetime of the prepared samples was calculated using a time-resolved photoluminescence spectrometer (FLuoTime 300). A 50-picosecond pulse duration laser source was used to excite the samples, and a nanosecond time-resolved camera was used to determine the time of charge carrier decay at the main emission peak of each sample.

Spectral responsivity and cutoff wavelength measurements

The spectral responsivity of the prepared p–i–n junctions was measured using a PVE300 system. A 75 W xenon lamp with a spectral range of 300–1100 nm and 1100–1800 nm was used. Two reference calibration detectors were used for the measurements: a silicon photodetector with a detection range of 300–1100 nm and a Ge photodetector with a detection range of 800–1800 nm.

Results and discussion

Impact of Pb, Sn, and As incorporation on Ge network strain determined using Raman spectroscopy

The large Sn, Pb, and As atoms dissolve in the Ge network and cause a modulation in the Γ direct valley and the L indirect valley in Ge. Another effect that enhances the directness of the Ge band gap is the tensile strain in the Ge network, as it alters the indirect valley energy and modulates the band gap.[15,16] Here, Pb, Sn, and As were dissolved in the Ge network by thermal treatment under vacuum. Raman spectroscopy measurements were carried out to investigate the strain in the Ge network due to Pb or Sn incorporation. Fig. 2 shows that there is a Raman peak due to the phonon mode of GeSn at 295 cm^{-1}. There is a lower shift in wavenumber compared to bulk Ge (at 300 cm^{-1}) because of the solubility of the large Sn atom (0.141 nm) in the Ge network.[17] Fig. 2 also shows a broad Raman peak due to the phonon mode of GePb at 254 cm^{-1}. This large shift to a lower wavenumber is due to the incorporation of larger Pb atoms (0.175 nm),[18] which causes high tensile strain. There is no peak observed for GeAs. The explanation for the disappearance of the GeAs mode is the high melting point of arsine (814 °C).[19] The GeAs can be obtained at a higher temperature than the annealing temperature of the prepared sample (400 °C). This causes more incorporation of Sn in the Ge network at such annealing temperature than Pb incorporation of large Pb atoms in the Ge network.[20]

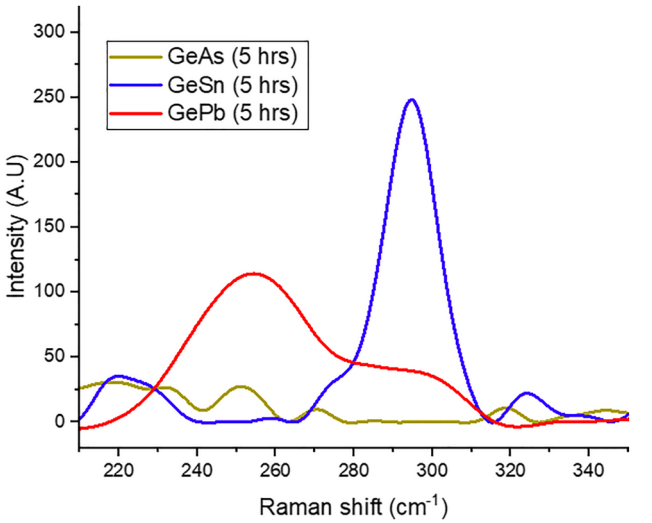

Fig. 2 Raman spectra of the prepared Ge thin films with As, Sn, and Pb contents annealed for 5 h.

X-ray diffraction

XRD analyses were carried out for the prepared samples to compare the strain in the Ge network caused by Pb, As and Sn content. Fig. 3 shows the XRD patterns of GePb-, GeSn-, and

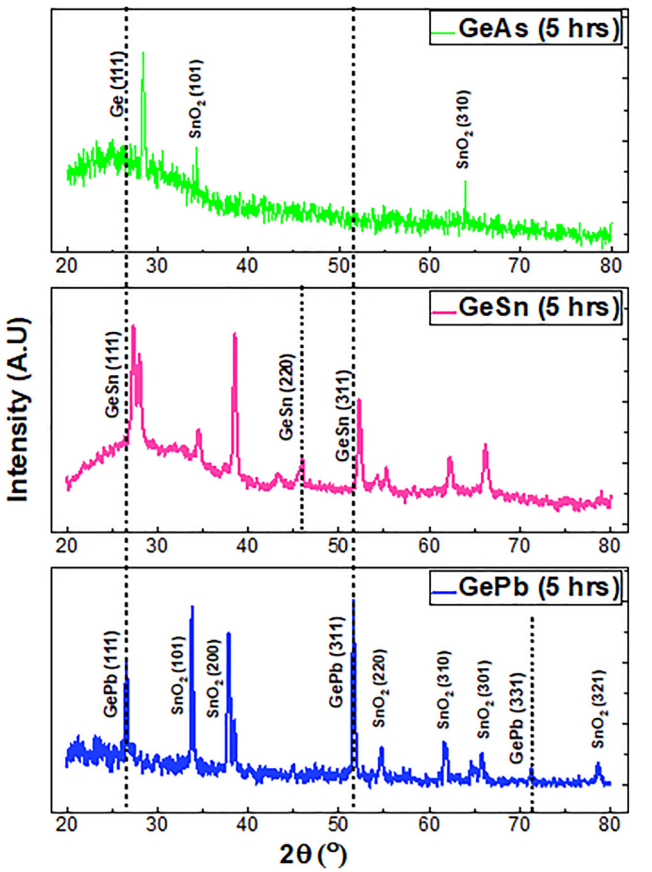

Fig. 3 XRD patterns of GePb-, GeSn-, and GeAs-based junctions annealed for 5 h.

Table 1 Lattice constant, *d*-spacing, and strain values of the strained Ge with Pb, Sn and As content grown under different directions

Sample	Orientation	*d*-Spacing (Å)	Lattice constant (Å)	FWHM β (°)	Strain (ε)
GePb (5 h)	GePb (111)	3.35	5.8	0.382	0.216
	GePb (311)	1.77	5.87	0.387	0.092
	GePb (331)	1.35	5.88	0.39	0.047
GeSn (5 h)	GeSn (111)	3.27	5.66	0.376	0.206
	GeSn (220)	1.97	6.57	0.348	0.142
	GeSn (311)	1.75	5.8	0.385	0.089
GeAs (5 h)	Ge (111)	3.24	5.61	0.331	0.172

GeAs-based junctions annealed for 5 h. It is observed that there are many strained Ge peaks as a result of Pb or Sn incorporation in different orientations, and only one Ge peak for As content. These strained Ge directions are (111), (311), and (331) at 2θ = 26.54°, 51.71°, and 71.34°, respectively, for the GePb-based sample (see JCPDS card No. 4-545).[21] The strained Ge growth orientations that appeared for the GeSn-based sample are (111), (220), and (311) at 2θ = 27.28°, 45.96°, and 52.33°, respectively (see JCPDS card No. 01-089-5011).[22] Only one peak is observed for the Ge grown crystallites in the (111) direction for the GeAs-based junction at 2θ = 28.43°. It is also observed that some peaks of SnO_2 appear at directions (101), (200), (220), (310), (301), and (321) (see JCPDS card No. 01-0657)[23] for both GePb- and GeSn-based samples, as they are prepared on the FTO substrate. The lattice constants and *d*-spacing of the strained Ge at different orientations were calculated using Bragg's equation $n\lambda = 2d\sin\theta$.[24] Deformations in the crystallization of Ge will occur as a result of Pb or Sn incorporation inside the Ge network. The relative deformation is known as strain, and it is equivalent to variations in the *d*-spacing. Strain ε in Ge structures doped with Sn, As, and Pb is quantified using the Williamson–Hall formula:[25]

$$\varepsilon = \frac{\beta}{4 \cdot \tan\theta} \quad (1)$$

Here, β and θ are the full-width-at-half-maximum and the diffraction angles of the XRD peaks, respectively. Table 1 summarizes the lattice constants, *d*-spacing, and strain of the strained Ge grown under different directions.

From their positions, it is seen that the diffraction peaks corresponding to the grown Ge crystallites with Pb content in directions (111) and (311) shift to lower diffraction angles compared to those of the grown Ge crystallites with Sn or As contents in the same directions. This lower shift in 2θ values and larger lattice constant values of GePb crystallites confirm that the GePb crystallites are more expanded and have higher tensile strain compared to the GeSn,[26] as discussed in the Raman spectroscopy analysis. The lattice constant values (see Table 1) show that the GePb crystallites have larger values of

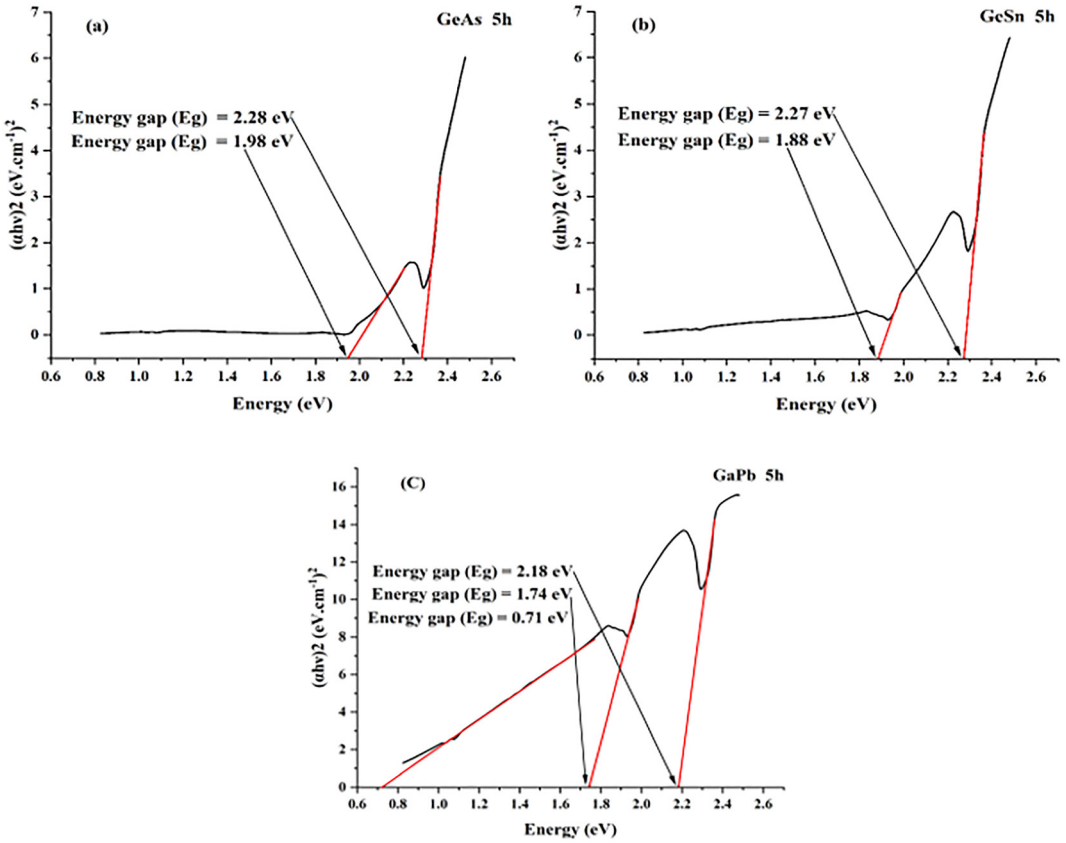

Fig. 4 Plots of $h\nu$ against $(\alpha h\nu)^2$ for the (a) GeAs, (b) GeSn, and (c) GePb thin films annealed for 5 h at 400 °C.

Table 2 The direct transitions of the prepared samples

Sample	Time annealing (h)	1st transition (eV)	2nd transition (eV)	3rd transition (eV)
GePb	1	0.62 (GePb)	1.76 (Ge nano particles)	2.21 (GeO_x)
GePb	3	0.62 (GePb)	1.75 (Ge nano particles)	2.17 (GeO_x)
GePb	5	0.71 (GePb)	1.74 (Ge nano particles)	2.18 (GeO_x)
GeSn	5	—	1.88 (Ge nano particles)	2.27 (GeO_x)
GeAs	5	—	1.98 (Ge nano particles)	2.28 (GeO_x)

5.8 Å corresponding to the (111) orientation and 5.88 Å corresponding to the (311) orientation compared to GeSn crystallites, with lattice constant values of 5.66 Å and 5.8 Å for the (111) and (311) orientations, respectively. The lattice constant of the grown Ge crystallites with As content is 5.61 Å, which is approximately the same as the lattice constant of pure germanium.[30] This indicates that As is not incorporated inside the Ge network. This is due to the high melting point of arsine (814 °C),[19] which is higher than the annealing temperature of the prepared sample (400 °C). This annealing temperature cannot initiate the incorporation of As inside the Ge network. The calculated strain values, summarized in Table 1, show that the strain value of the GePb crystallites for the (111) orientation is 0.216. The strain value of GeSn crystallites for the (111) orientation is 0.206. The strain value of Ge crystallites of As for the (111) orientation is 0.172. This indicates that the Pb incorporation inside the Ge network causes higher tensile strain than Sn and As, which causes a modulation of the indirect Ge band gap to the direct one.

Direct band gap investigation using UV-vis-NIR spectroscopy measurements

UV-Vis-NIR spectroscopy measurements were carried out to investigate the band gap modulation of Ge from indirect to direct. This modulation was obtained because of the separate incorporation of tin, arsine, and lead content in the Ge network. We made a comparison between the impacts of Sn, As, and Pb contents in the Ge network and their impact on the Ge band gap. We also compared the different annealing times of Ge with Pb content to illustrate the effect of increased solubility of Pb in the Ge network on the band gap value of the GePb alloy. From the absorbance data, we calculated the absorption coefficient α, using the following equation:[27]

$$\alpha = 2.303\frac{A}{t} \quad (2)$$

where A is the absorbance, and t is the thickness of the sample.

We applied Tauc plot to investigate the direct band gap of Ge. The Tauc plot exhibited a linear fitting when $h\nu$ was plotted against $(\alpha h\nu)^2$, as shown in Fig. 4. This confirmed the direct band gap of Ge with the different As, Sn, and Pb contents.[28,29]

Fig. 4 shows that the GePb sample absorbs more than GeAs and GeSn. This gives GePb a good chance for optoelectronic and photonic applications rather than GeSn and GeAs.[3] Fig. 4(a)–(c) showed that the samples have two band gap values. The transition value in the range 2.18 eV–2.28 eV corresponds to GeO due to oxidation of Ge during the low-vacuum annealing.[30,31] The transition value in the range of 1.74 eV–1.94 eV corresponds to Ge incorporated with As, Sn, and Pb, separately.[32] It is seen that the GePb sample with Pb incorporated in the Ge network has a lower band gap value (0.71 eV) than the GeSn and GeAs samples, as shown in the band gap values of the three samples in Fig. 4(a)–(c). This makes GePb alloys suitable for application in IR photonics and optoelectronics.[33]

Fig. 4(c) and 5 show a plot of $h\nu$ against $(\alpha h\nu)^2$ for GePb thin films annealed for annealing times of 1, 3, and 5 h, respectively. The figures show an insignificant variation in the band gap values owing to the increase in annealing time from one to five hours, with the band gap values decreasing by 0.03 eV (Table 2).

Photoluminescence measurements

PL measurements were carried out to determine the transitions of the prepared samples. Fig. 6(a) and (b) shows the emission peaks of the prepared Ge thin films with As, Sn, and Pb contents annealed for 5 h. It is seen that there are two emission peaks of the prepared sample at 563 nm and 750 nm. They coincide with the transitions at ≈2.2 eV and 1.7 eV obtained from the UV-vis-NIR spectroscopy absorbance measurements. This observed blue shift of the emission peak values is due to the oxidation under low-vacuum annealing during the MIC process. It is observed that the GePb sample has higher emissions than the GeAs and GeSn samples. A red shift is observed

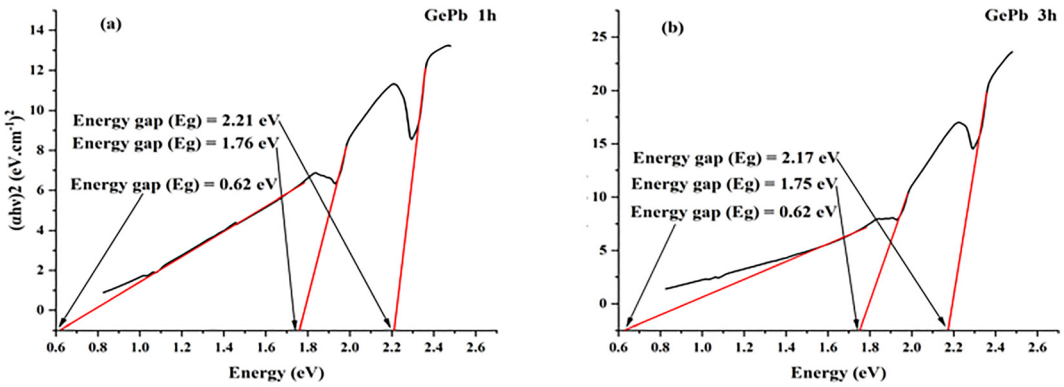

Fig. 5 Plots of $h\nu$ against $(\alpha h\nu)^2$ for the GePb thin films annealed for annealing times of (a) 1 and (b) 3 h at 400 °C.

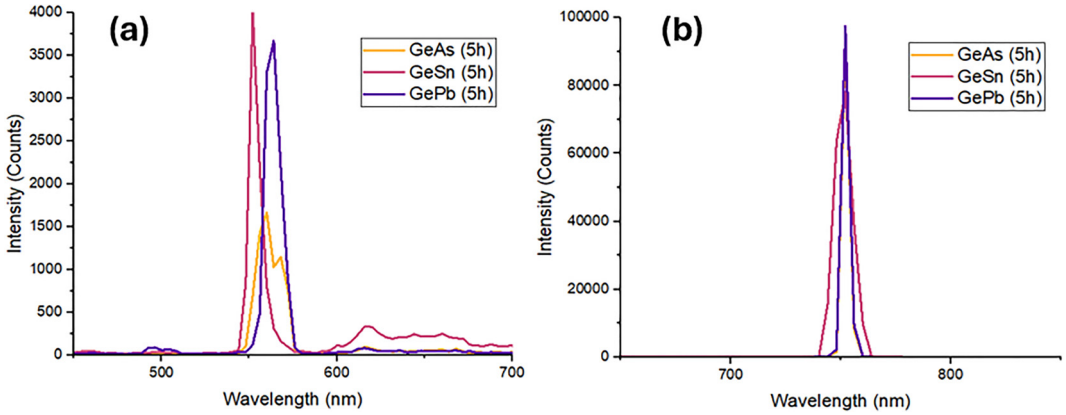

Fig. 6 Photoluminescence emission spectra of the prepared Ge thin films with As, Sn, and Pb contents annealed for 5 h, (a) in visible, (b) in NIR region of spectra.

at the emission peaks of the GePb sample, which matches the UV-vis-NIR spectroscopy analysis as the value of the GePb band gap is red-shifted compared to the GeSn and GeAs samples.

I–V characteristics of the prepared junction under dark conditions

The *I–V* characteristics of the prepared junction were measured with a Metrohm Autolab 87070 potentiostat under dark conditions in the range ±2 V. The junction parameters were calculated using the Schottky equation:[34]

$$I_D = I_S\left[e^{\frac{eV}{nKT}} - 1\right] \quad (3)$$

where I_D is the dark reverse current, I_S the saturation current, e is the charge of the electron, V is the applied potential, n is the

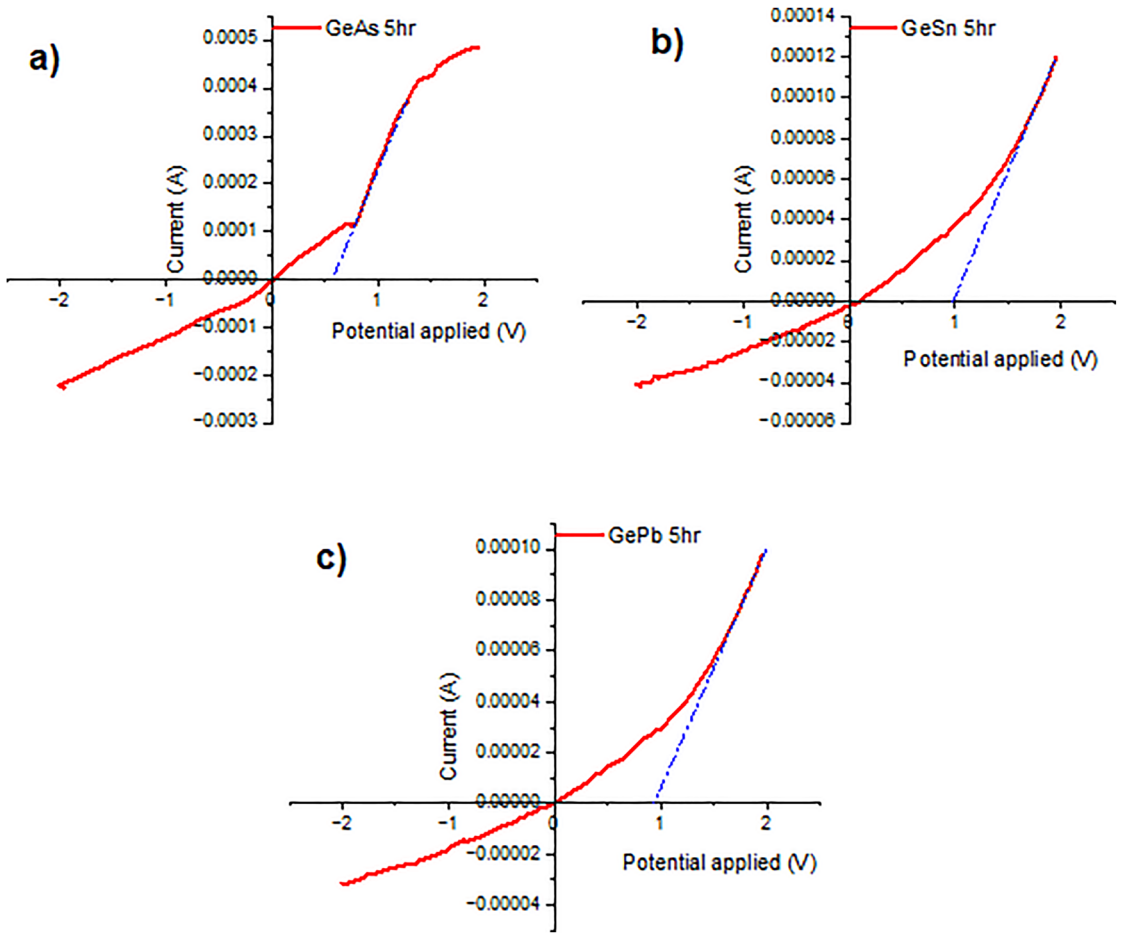

Fig. 7 Plots of current *I* against the applied potential *V* for the (a) GeAs-, (b) GeSn-, and (c) GePb-based p–i–n junctions.

ideality factor, K is the Boltzmann constant, and T is the operating temperature in Kelvin.

Fig. 7 and 8 show the current I plotted against the applied potential V. The turn-on voltage was determined from the intercept of the linear fit of the forward biasing plot with the x-axis. The turn-on voltage of the prepared junctions is listed in Table 1. It is equal to 0.59 V for the GeAs-based p–i–n junction, due to the low solubility of As in the Ge network as described in the discussion of the Raman measurements. This metal reduces the depletion of the diode. The turn-on voltage of the GePb- and GeSn-based p–i–n junctions is around 1 V. The turn-on voltage of the GePb-based p–i–n junctions varies from 1.12 V to 0.94 V as the annealing time increases from 1 h to 5 h. As the annealing time increases, the incorporation of Pb in the Ge network increases, and a reduction in the depletion region occurs.[35] The dark current values were determined from the reverse biasing plot. The dark current value at reverse biasing voltage ($V = -2$ V) was 2.22×10^{-4} A for the GeAs-based junction. This value is considered a high value of dark current, because of the remaining low solubility as metal that doesn't incorporate in Ge network.[36] This increases the thermally diffused backward current. Fig. 9 and 10 show the plot of $\ln(I)$ against the biasing voltage V. The slope of the graph in both regions 1 and 2 is equal to e/nKT, and the ideality factor of the diodes is calculated using the Schottky equation.[37] As a result of high dark current, the ideality factor of this junction (n) for the low-voltage region (region 1) is equal to 2.06, which is far from the ideal diode factor of 1.[38]

It is observed that the GePb-based p–i–n junction has a lower dark current of 3.16×10^{-5} A compared to those of GeSn- and GeAs-based junctions, and, hence, the ideality factor in the low-voltage region is 1.146, which is very close to the ideal value. The ideality factor of the GeSn-based junction is 1.57, which is far from the ideal value. This makes the GePb alloy more suitable for Ge-based junction fabrication than GeSn. It is also observed that the dark current value decreases and thus the ideality factor approaches the ideal value for the GePb-based junction with increasing annealing time from 1 h to 5 h. This is due to the increased incorporation of Pb inside the Ge network, which reduces the metal clusters that cause the conduction electrons of Pb to contribute to backward diffusion current.[39]

The calculated ideality factor for region 2 varied greatly from 26.95 to 141.6. These values, which are very far from the ideal value, arise because the high applied voltage causes tunneling of the conduction electrons of the metals As, Sn and Pb.[40] Table 3 summarizes the calculated parameters of the prepared junctions.

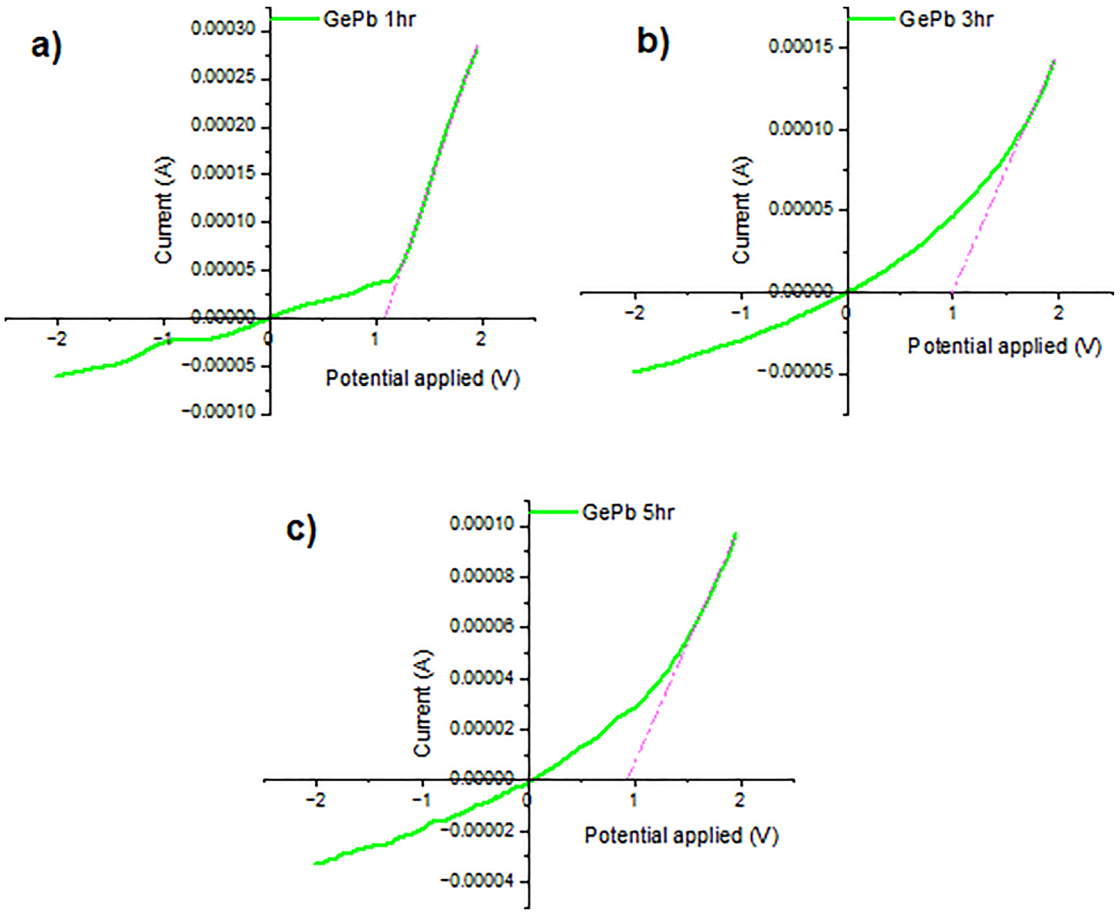

Fig. 8 Plot of current I against the applied potential V for the GePb-based p–i–n junctions annealed for (a) 1 h, (b) 3 h, and (c) 5 h.

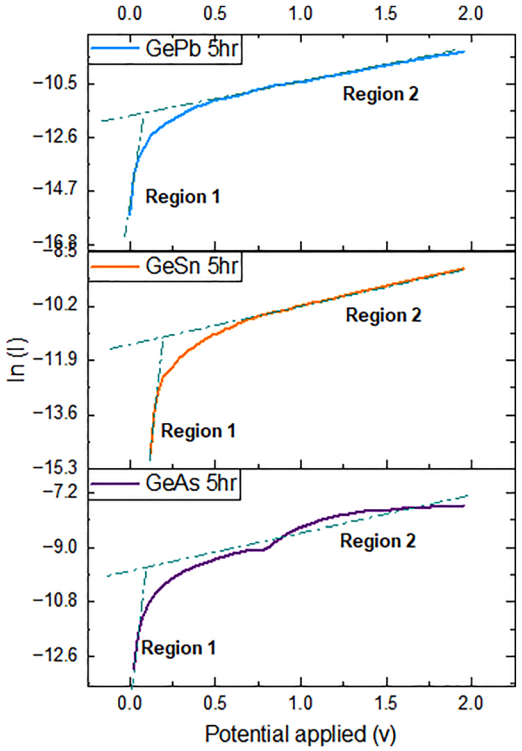

Fig. 9 Plot of ln(*I*) against the applied potential *V* for the fabricated GeAs, GeSn, and GePb based p–i–n junctions.

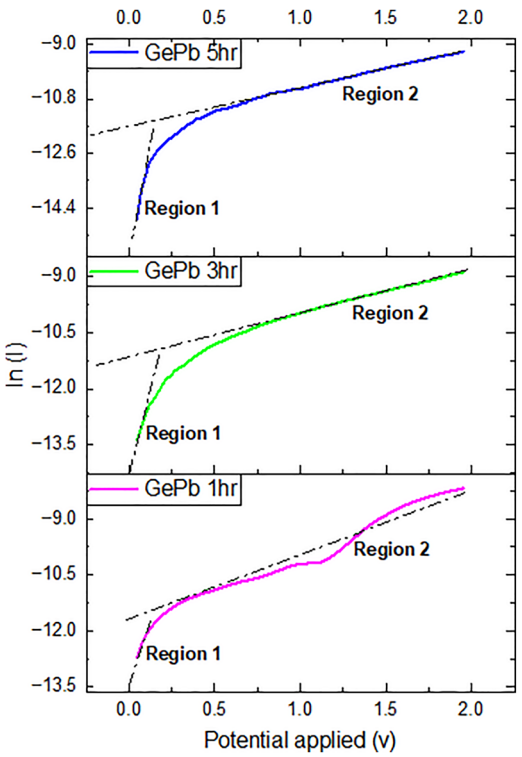

Fig. 10 Plot of ln(*I*) against the applied potential *V* for the GePb based p–i–n junctions annealed for 1 h, 3 h, and 5 h.

Table 3 The calculated parameters of the prepared junctions

Sample	Parameter			
	Turn-on voltage (V)	I_D (A)	n	
			Region 1	Region 2
n-FTO/GeAs/Al-GeAs (5 h)	0.59	2.22×10^{-4}	2.06	141.6
n-FTO/GeSn/Al-GeSn (5 h)	1	4.11×10^{-5}	1.57	33.86
n-FTO/GePb/Al-GePb (5 h)	0.94	3.16×10^{-5}	1.146	32.7
n-FTO/GePb/Al-GePb (3 h)	0.99	4.91×10^{-5}	2.11	34.01
n-FTO/GePb/Al-GePb (1 h)	1.12	6.03×10^{-5}	2.15	26.95

Charge carrier lifetime measurements

Charge carrier lifetime measurements of the prepared samples were obtained using the time-resolved photoluminescence technique. Fig. 11 shows the charge carrier lifetime of the GeAs-based p–i–n junction annealed for 5 h, the GeSn-based p–i–n junction annealed for 5 h, and the GePb-based p–i–n junction annealed for 1 h, 3 h, and 5 h. It is observed that the GePb-based p–i–n junctions annealed for different times have higher charge carrier lifetimes (4.64 ns) than the GeSn-based p–i–n junction, which has a carrier lifetime of 4.53 ns. This higher charge carrier lifetime value makes the fabricated GePb-based p–i–n junction a promising semiconductor junction that can be utilized in efficient optoelectronic devices rather than GeSn.

Photoresponsivity measurements of the prepared junctions

Photoresponsivity measurements were carried out to investigate the detection region of the prepared p–i–n GePb-based junctions compared to the GeAs- and GeSn-based junctions. The spectral responsivity of the prepared heterojunctions was measured using a PVE300 system with 75 W xenon and quartz halogen lamps with spectral ranges of 300–1100 nm and 1100–2500 nm, respectively. Fig. 10 shows the photoresponsivity of the prepared GeAs-, GeSn-, and GePb-based p–i–n junctions annealed for 5 h. The measurements reveal that the prepared heterostructures have a response near the UV portion of radiation, as seen in Fig. 12. This can be explained by considering that the Ge networks doped with Pb, Sn, or As in the prepared samples contain oxygen vacancies forming GeO_x, owing to the heat treatment under low-vacuum conditions. Germanium oxide has a wide band gap that pushes UV spectrum to generate photocurrent as discussed in photoluminescence and UV-vis spectroscopy.

Fig. 12 shows that the response decreases from the near UV region to the visible, with a cut-off wavelength of 550 nm. This allows the prepared p–i–n GeSn heterojunction to be utilized as a UV photodetector. The responsivity then increases in the NIR region from 700 nm to 1200 nm. This response in the NIR region corresponds to the Ge doped with As, Sn, or Pb metals. It is seen that the responsivity of the GePb-based junction then increases to a high value from 1500 nm to 1800 nm. We could not measure the responsivity at wavelengths longer than 1800 nm due to the limits of the responsivity system. However, from the UV-vis-NIR spectroscopy measurements, we could

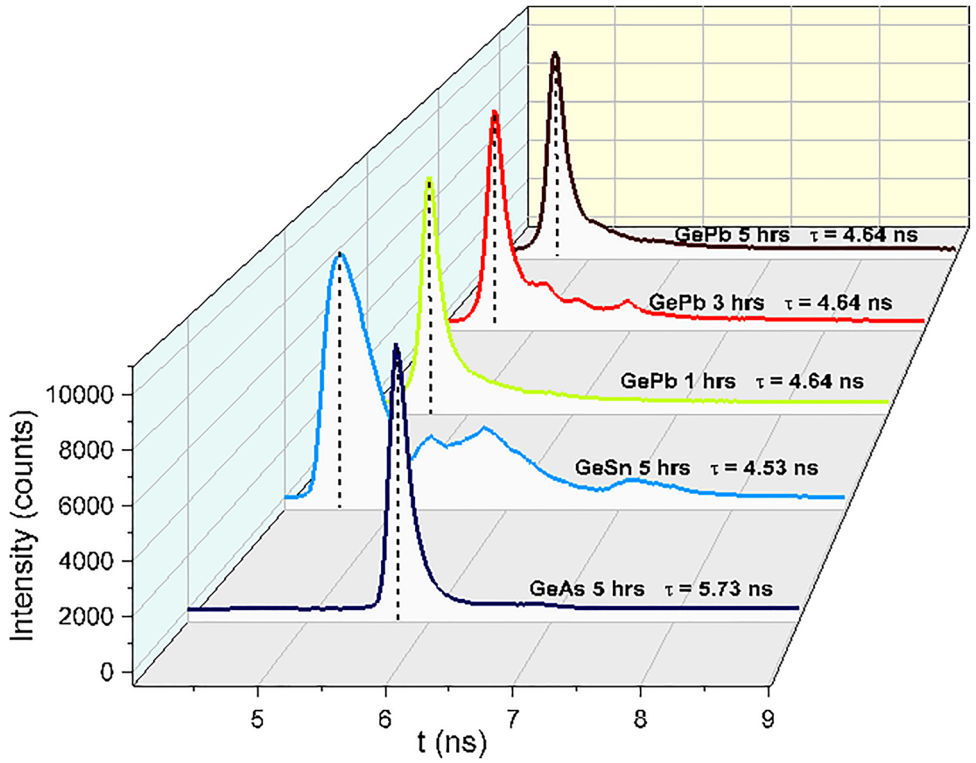

Fig. 11 Time-resolved photoluminescence of the GeAs-based p–i–n junction annealed for 5 h, the GeSn-based p–i–n junction annealed for 5 h, and the GePb-based p–i–n junction annealed for 1 h, 3 h, and 5 h.

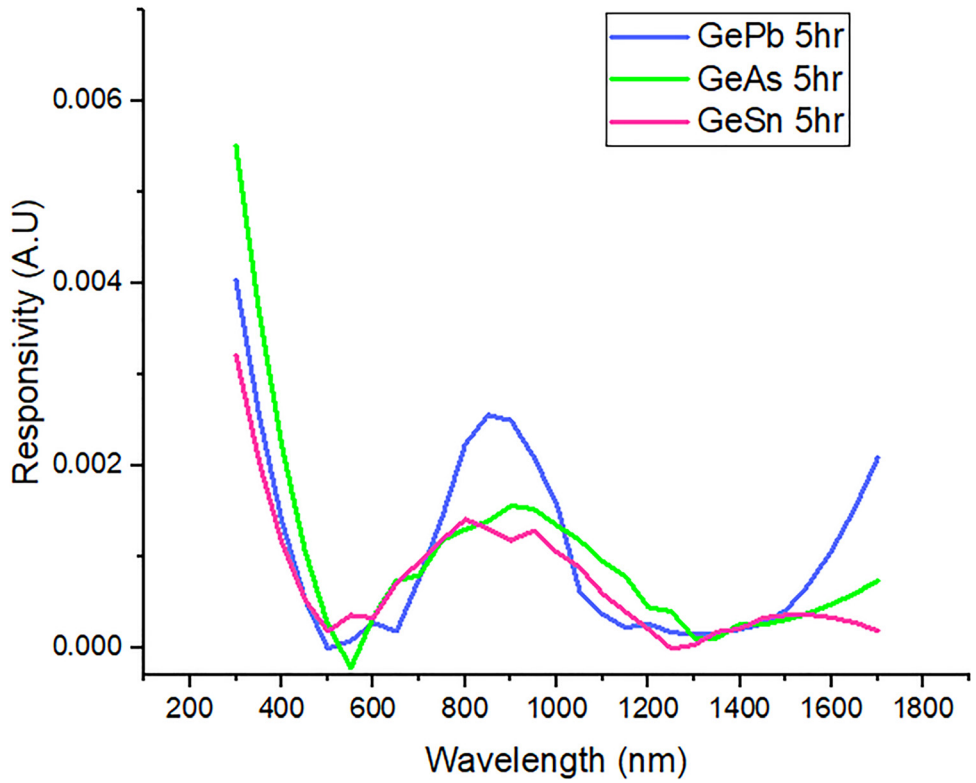

Fig. 12 The photoresponsivity of the prepared GeAs-, GeSn-, and GePb-based p–i–n junctions annealed for 5 h.

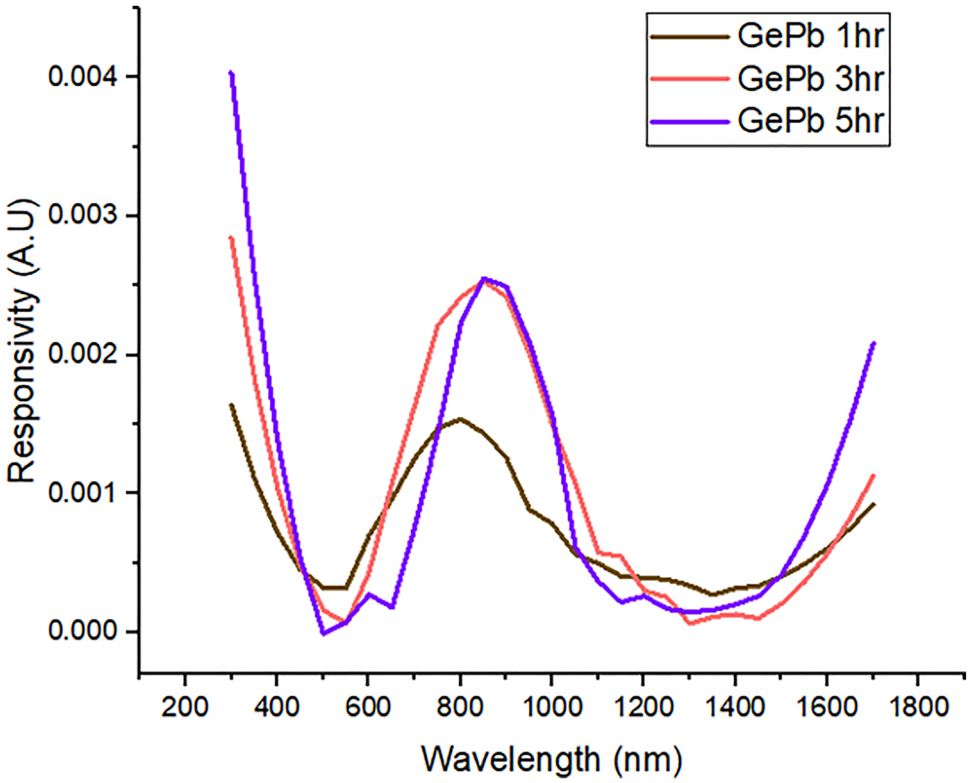

Fig. 13 The photoresponsivity of the prepared GePb-based p–i–n junctions annealed for 1, 3, and 5 h.

estimate that there will be a peak at 2000 nm. This increase in the responsivity over the NIR-IR region is because the Pb content reduces the Ge band gap to very low values.[41] This makes the GePb alloy more suitable than the GeSn compound for the fabrication of Ge-based photodetectors in the NIR and Mid-IR regions.[42]

We demonstrated the photoresponse of the GePb-based p–i–n junctions annealed for different annealing times (1, 3, and 5 h) to investigate the impact of increasing Pb incorporation inside the Ge network on the photoresponsivity. Fig. 13 shows the photoresponsivity of the prepared GePb-based p-junctions annealed for 1, 3, and 5 h. It is observed that the responsivity of the GePb-based p-junctions annealed for 1 h is lower than that annealed for 5 h. The increase in the annealing time from 1 to 5 h enhances the responsivity because Pb metal is incorporated with higher ratios with higher annealing times. This enhances the direct transition in Ge with higher Pb content[43] and the photocurrent and photoresponsivity increase. It is seen that the cut-off wavelengths in different regions of the spectrum are shifted toward longer wavelengths with higher annealing time. This is due to the incorporation of Pb metal inside the Ge network, which reduces the band gap. This work is the first trial to fabricate a GePb p–i–n photodetector *via* a MIC process that can operate in both UV and NIR regions.

Conclusion

In our work, we compared Ge networks containing different contents of As, Sn, and Pb. Thin films of the semiconductor and metal layers were thermally deposited under a vacuum of 4.6×10^{-5} mbar. A 50 nm layer of As, Sn, and Pb was deposited separately on FTO substrates, then each metal layer was covered with 500 nm of Ge, followed by 10 nm of Al as a p-dopant on Ge/(metal layer) above n-type FTO substrates. The deposited films were then annealed under low-vacuum conditions (5.4×10^{-2} bar) at 400 °C. The Ge/As layers were annealed for 5 hours, the Ge/Sn layers were annealed for 5 hours, and the Ge/Pb layers were annealed for 1, 3, and 5 hours. The p–i–n junctions were formed *via* MIC. Raman spectroscopy showed a peak due to the phonon mode of GePb at 254 cm^{-1}. This large shift to a lower wavenumber is due to the incorporation of a larger Pb atom (0.175 nm), which causes higher tensile strain compared to the GeSn-based sample (Sn radius 0.141 nm), which has a lower peak shift at 295 cm^{-1}. XRD measurements reveal that GePb crystallites have larger lattice constants of 5.8 Å, corresponding to the (111) orientation and so higher tensile strain compared to the Ge crystallite lattice constant, with Sn and As values of 5.66 Å and 5.61 Å for (111) orientations, respectively. UV-Vis-NIR spectroscopy revealed that the samples have two band gap values. The transition value at a range of 2.18 eV–2.28 eV corresponds to GeO, as a result of the oxidation of Ge during the low-vacuum annealing. The transition value in the range of 1.74 eV–1.94 eV corresponds to Ge doped with As, Sn, and Pb, separately. GePb has a third transition at 0.6 eV. It is observed that the GePb-based p–i–n junction has a lower dark current of 3.16×10^{-5} A compared to those of the GeSn- and GeAs-based junctions, and, hence, the ideality factor in the low

voltage region is 1.146, which is very close to the ideal value. The ideality factor of the GeSn-based junction is 1.57, which is far from the ideal value. Time-resolved PL measurements showed that the GePb-based junction has a charge carrier lifetime of 4.64 ns, whereas the corresponding value for the GeSn-based junction is 4.53 ns. The photoresponsivity measurements reveal that the prepared heterostructures have a response near the UV region due to oxygen vacancies forming GeO_x because of the heat treatment under low-vacuum conditions. The material can thus be used as a photodetector in the UV region. The responsivity then increases in the NIR region from 700 nm to 1200 nm. This response in the NIR region corresponds to the Ge doped with As, Sn, or Pb metals. The responsivity of the GePb-based junction then increases to a high value from 1500 nm again compared to GeSn-based junctions because the Pb content reduces the Ge band gap to very low values, as confirmed by UV-vis spectroscopy analysis. This demonstrates for the first time that the GePb-based junctions are more suitable than GeSn alloys for the fabrication of Ge-based photodetectors operating in both the UV and NIR-IR regions and opens the way for GePb alloys to replace GeSn in future optoelectronic applications.

Conflicts of interest

The authors declare no competing interests or non-financial interests.

Data availability

The data that support the plots and results within this paper are available from the corresponding authors upon reasonable request.

Acknowledgements

We greatly thank the Physics Department, Faculty of Science, Menoufia University; Kafrelsheikh University; the City of Scientific Research and Technological Applications, the Advanced Materials Institute; and the Central Metallurgical Research & Development Institute (CMRDI) for their support with the preparation and measurement techniques of this work.

References

1 D. Marris-Morini, P. Chaisakul, M. S. Rouifed, J. Frigerio, G. Isella, D. Chrastina and L. Vivien Low energy consumption and high speed germanium-based optoelectronic devices. In The European Conference on Lasers and Electro-Optics, Optica Publishing Group, 2013, p. CI_2_3.

2 S. An, H. Park and M. Kim, Recent advances in single crystal narrow band-gap semiconductor nanomembranes and their flexible optoelectronic device applications: Ge, GeSn, InGaAs, and 2D materials, *J. Mater. Chem. C*, 2023, **11**(7), 2430–2448.

3 M. A. Nawwar, M. S. A. Ghazala, L. M. S. El-Deen and A. E. H. B. Kashyout, Impact of strain engineering and Sn content on GeSn heterostructured nanomaterials for nanoelectronics and photonic devices, *RSC Adv.*, 2022, **12**(38), 24518–24554.

4 J. S. C. Jang and C. C. Koch, Melting and possible amorphization of Sn and Pb in Ge/Sn and Ge/Pb mechanically milled powders, *J. Mater. Res.*, 1990, **5**(2), 325–333.

5 Q. Zhou, T. K. Chan, S. L. Lim, C. Zhan, T. Osipowicz, X. Gong and Y. C. Yeo, Single crystalline germanium-lead alloy on germanium substrate formed by pulsed laser epitaxy, *ECS Solid State Lett.*, 2014, **3**(8), P91.

6 M. C. Weiser, D. Schwarz, H. S. Funk, D. Weißhaupt, C. Serra, J. Schulze and S. Chiussi Fabrication of GePb-alloys by means of pulsed laser induced epitaxy. In 2019 42nd International Convention on Information and Communication Technology, Electronics and Microelectronics (MIPRO), IEEE, 2019, pp. 1–6.

7 X. Liu, J. Zheng, L. Zhou, Z. Liu, Y. Zuo, C. Xue and B. Cheng, Growth of single crystalline GePb film on Ge substrate by magnetron sputtering epitaxy, *J. Alloys Compd.*, 2019, **785**, 228–231.

8 J. Yang, H. Hu, Y. Miao, B. Wang, W. Wang, H. Su and Y. Ma, Single-crystalline GePb alloys formed by rapid thermal annealing-induced epitaxy, *J. Phys. D: Appl. Phys.*, 2020, **53**(26), 265105.

9 H. Alahmad, A. Mosleh, M. Alher, S. F. Banihashemian, S. A. Ghetmiri, S. Al-Kabi and H. A. Naseem, GePb alloy growth using layer inversion method, *J. Electron. Mater.*, 2018, **47**, 3733–3740.

10 X. Liu, J. Zheng, Q. Huang, Y. Pang, D. Zhang, Y. Zhu and B. Cheng, Growth and characterization of GePb/Ge multiple quantum wells, *J. Alloys Compd.*, 2023, **934**, 167954.

11 W. Huang, B. Cheng, C. Xue and C. Li, Comparative studies of clustering effect, electronic and optical properties for GePb and GeSn alloys with low Pb and Sn concentration, *Phys. B*, 2014, **443**, 43–48.

12 S. Xia, J. Yu, J. Wang, W. Huang, Y. Wen, C. Li and S. Chen, A first-principle study on the band structure of GePb alloys, *Semicond. Sci. Technol.*, 2024, **39**(12), 125020.

13 X. Liu, J. Zheng, X. Li, Z. Liu, Y. Zuo, C. Xue and B. Cheng, Study of GePb photodetectors for shortwave infrared detection, *Opt. Express*, 2019, **27**(13), 18038–18043.

14 J. Yu, G. Lin, S. Xia, W. Huang, T. Yang, J. Jiao and J. Li, P–i–n photodetector with active GePb layer grown by sputtering epitaxy, *Appl. Phys. Express*, 2024, **17**(4), 045501.

15 Z. Qi, H. Sun, M. Luo, Y. Jung and D. Nam, Strained germanium nanowire optoelectronic devices for photonic-integrated circuits, *J. Phys.: Condens. Matter*, 2018, **30**(33), 334004.

16 C. Y. Lin, H. Y. Ye, F. L. Lu, H. S. Lan and C. W. Liu, Biaxial strain effects on photoluminescence of Ge/strained GeSn/Ge quantum well, *Opt. Mater. Express*, 2018, **8**(9), 2795–2802.

17 C. S. Cook, *Growth and optical properties of novel doped and undoped group IV materials based on silicon, germanium, and tin*, Arizona State University, 2006.

18 Y. L. Wang, L. Cai and Y. Xia, Monodisperse spherical colloids of Pb and their use as chemical templates to produce hollow particles, *Adv. Mater.*, 2005, **17**(4), 473–477.
19 N. A. Gokcen, The As (arsenic) system, *Bull. Alloy Phase Diagrams*, 1989, **10**(1), 11–22.
20 L. H. Robins, D. L. Kaiser, L. D. Rotter, P. K. Schenck, G. T. Stauf and D. Rytz, Investigation of the structure of barium titanate thin films by Raman spectroscopy, *J. Appl. Phys.*, 1994, **76**(11), 7487–7498.
21 Z. Gu, F. Liu, J. Y. Howe, M. P. Paranthaman and Z. Pan, Germanium-catalyzed hierarchical Al2O3 and SiO2 nanowire bunch arrays, *Nanoscale*, 2009, **1**(3), 347–354.
22 H. Li, J. Brouillet, A. Salas, X. Wang and J. Liu, Low temperature growth of high crystallinity GeSn on amorphous layers for advanced optoelectronics, *Opt. Mater. Express*, 2013, **3**(9), 1385–1396.
23 N. Wan, X. Lu, Y. Wang, W. Zhang, Y. Bai, Y. S. Hu and S. Dai, Improved Li storage performance in SnO2 nanocrystals by a synergetic doping, *Sci. Rep.*, 2016, **6**(1), 18978.
24 B. Greenberg, Bragg's law with refraction, *Found. Crystallogr.*, 1989, **45**(3), 238–241.
25 A. A. Akl and A. S. Hassanien, Microstructure and crystal imperfections of nanosized CdSxSe1−x thermally evaporated thin films, *Superlattices Microstruct.*, 2015, **85**, 67–81.
26 K. R. Desai, S. T. Alone, S. R. Wadgane, S. E. Shirsath, K. M. Batoo, A. Imran and R. H. Kadam, X-ray diffraction based Williamson–Hall analysis and Rietveld refinement for strain mechanism in Mg–Mn co-substituted CdFe2O4 nanoparticles, *Phys. B*, 2021, **614**, 413054.
27 K. N. Manjunatha and S. Paul, Investigation of optical properties of nickel oxide thin films deposited on different substrates, *Appl. Surf. Sci.*, 2015, **352**, 10–15.
28 L. Dejam, S. Kulesza, J. Sabbaghzadeh, A. Ghaderi, S. Solaymani, Ş. Ţălu and A. Hossein Sari, ZnO, Cu-doped ZnO, Al-doped ZnO and Cu-Al doped ZnO thin films: Advanced micro-morphology, crystalline structures and optical properties, *Results Phys.*, 2023, **44**, 106209.
29 K. D. Singh, R. Pandit and R. Kumar, Effect of rare earth ions on structural and optical properties of specific perovskite orthochromates; RCrO3 (R = La, Nd, Eu, Gd, Dy, and Y), *Solid State Sci.*, 2018, **85**, 70–75.
30 M. A. Nawwar, M. S. Abo Ghazala, L. M. Sharaf El-Deen, A. El-Shaer, B. Anis and A. E. H. Bashir Kashyout, Toward White Light Random Lasing Emission Based on Strained Nano Polygermanium Doped with Tin *via* Metal-Induced Crystallization (MIC), *Cryst. Growth Des.*, 2022, **23**(2), 751–768.
31 M. Zacharias and P. M. Fauchet, Blue luminescence in films containing Ge and GeO 2 nanocrystals: the role of defects, *Appl. Phys. Lett.*, 1997, **71**(3), 380–382.
32 V. Kumar and Y. Kawazoe, Hydrogenated caged clusters of Si, Ge, and Sn and their endohedral doping with atoms: Ab initio calculations, *Phys. Rev. B:Condens. Matter Mater. Phys.*, 2007, **75**(15), 155425.
33 J. Yu, G. Lin, S. Xia, W. Huang, T. Yang, J. Jiao and J. Li, P–i–n photodetector with active GePb layer grown by sputtering epitaxy, *Appl. Phys. Express*, 2024, **17**(4), 045501.
34 P. Kaushal, S. Chand and J. Osvald, Current–voltage characteristics of Schottky diode simulated using semiconductor device equations, *Int. J. Electron.*, 2013, **100**(5), 686–698.
35 D. Wang, Y. L. Chang, Q. Wang, J. Cao, D. B. Farmer, R. G. Gordon and H. Dai, Surface chemistry and electrical properties of germanium nanowires, *J. Am. Chem. Soc.*, 2004, **126**(37), 11602–11611.
36 P. Huo, I. Lombardero, I. García and I. Rey-Stolle, Enhanced performance of GaInP/GaAs/Ge solar cells under high concentration through Pd/Ge/Ti/Pd/Al grid metallization, *Prog. Photovoltaics Res. Appl.*, 2019, **27**(9), 789–797.
37 S. Yoo, W. J. Potscavage Jr, B. Domercq, S. H. Han, S. C. Jones, R. Szoszkiewicz and B. Kippelen, Analysis of improved photovoltaic properties of pentacene/C60 organic solar cells: Effects of exciton blocking layer thickness and thermal annealing, *Solid-State Electron.*, 2007, **51**(10), 1367–1375.
38 J. R. Sites and P. H. Mauk, Diode quality factor determination for thin-film solar cells, *Sol. Cells*, 1989, **27**(1–4), 411–417.
39 F. X. Xiao, Z. Zeng and B. Liu, Bridging the gap: electron relay and plasmonic sensitization of metal nanocrystals for metal clusters, *J. Am. Chem. Soc.*, 2015, **137**(33), 10735–10744.
40 M. A. Nawwar, M. S. A. Ghazala, L. M. S. El-Deen, B. Anis, A. El-Shaer, A. M. Elseman and A. E. H. B. Kashyout, Controlling barrier height and spectral responsivity of p–i–n based GeSn photodetectors *via* arsenic incorporation, *RSC Adv.*, 2023, **13**(14), 9154–9167.
41 C. Claeys, E. Simoen, C. Claeys and E. Simoen, *Gettering and Passivation of Metals in Silicon and Germanium. Metal Impurities in Silicon-and Germanium-Based Technologies: Origin, Characterization, Control, and Device Impact*, 2018, pp. 351–388.
42 P. Xiao, Z. Zhang, J. Ge, Y. Deng, X. Chen, J. R. Zhang and Y. Wang, Surface passivation of intensely luminescent all-inorganic nanocrystals and their direct optical patterning, *Nat. Commun.*, 2023, **14**(1), 49.
43 J. Doherty, S. Biswas, E. Galluccio, C. A. Broderick, A. Garcia-Gil, R. Duffy and J. D. Holmes, Progress on germanium–tin nanoscale alloys, *Chem. Mater.*, 2020, **32**(11), 4383–4408.